Forced wave propagation and energy distribution in anisotropic laminate composites

Evgeny Glushkov,[a] Natalia Glushkova, and Artem Eremin
Institute for Mathematics, Mechanics and Informatics, Kuban State University, Krasnodar 350040, Russia

(Received 28 July 2010; revised 4 February 2011; accepted 4 February 2011)

Elastodynamic response of anisotropic laminate composite structures subjected to a force loading is evaluated based on the integral representations in terms of Green's matrices. Explicit and asymptotic expressions for guided waves generated by a given source are then obtained from those integrals by means of series expansions and the residue technique. Unlike to conventional modal expansions, such representations keep information about the source, giving an opportunity for a quantitative near- and far-field analysis of generated waves. An effective computer implementation is achieved by the use of fast and stable algorithms for the Green matrix, pole, and residue calculations. The potential of the model is demonstrated by examples of anisotropy manifestation in the directivity of radiated waves. The effect of main energy outflow in the direction of either upper- or inner-ply orientation depending on the source size and frequency is discussed.
 [DOI: 10.1121/1.3559699]

PACS number(s): 43.35.Pt, 43.35.Zc, 43.20.Rz, 43.20.Mv [ANN] Pages: 2923–2934

I. INTRODUCTION

Elastic guided waves (GWs) propagating in layered materials have been actively studied in applications such as seismology, ultrasonic inspection, material characterization, electromechanical devices, etc. Mathematical simulation of wave phenomena in laminate structures relies on the transfer matrix approach going back to the pioneering works by Thomson,[1] Haskell,[2] and Petrashen[3] in the 1950s. Subsequently, this approach has also been generalized for anisotropic laminates[4–6] and a number of results in this field have been reported.

There are two main directions for the use of transfer matrix algorithms: (1) in the context of modal analysis and (2) for Green's matrix calculation. In the first, the phase and group velocities, spatial eigenforms and dispersion characteristics of GWs are obtained from a homogeneous boundary value problem (BVP) without accounting for the wave source. With a wave source modeled by a surface load, i.e., by inhomogeneous boundary conditions, the generated wave field may be represented via the convolution of a Green's matrix for the laminate composite structure with a source function. In addition to the capabilities provided by modal analysis, a second way, referred to as integral approach, allows one to carry out quantitative amplitude and energy analysis of the GWs excited by a specific source.

The present paper examines the influence of anisotropy and lamination on forced wave energy radiation and its spatial directivity and modal partitioning based on the integral approach. In this context, the solution to the corresponding BVP derived in the form of inverse Fourier path integrals is reduced to explicit series expansions in terms of GWs expressed via one-dimensional integrals over the polar angular variable. Finally, asymptotic representations convenient for a far-field analysis are derived from those integrals. The expansion coefficients of these representations contain all required information about the source. In that way, the coupling procedures commonly required for hybrid schemes[7] are not needed.

We have chosen Refs. 8–11 as principal references from the variety of literature devoted to wave propagation in anisotropic plates. They are close analogs with regard to the objectives and/or the mathematical techniques used here. Reference 8 presents angular and dispersion characteristics of Lamb waves in laminate composites obtained using the modal analysis technique, while Ref. 9 contains examples of forced (laser-generated) GW energy behavior. We used those results for numerical testing and validation of our computer programs. References 10 and 11 deal with the integral equation based computer simulation of three-dimensional (3D) forced wave excitation in generally anisotropic composite plates. As a distinction, only through-plate transmitted waves are considered[10] (no GWs), while a far-field asymptotic solution to the 3D problem is derived in terms of modal solutions to the related two-dimensional (2D) problem,[11] unlike the direct derivation from the double-integral representation accomplished in the present paper.

The paper is organized as follows. After the mathematical formulation of the BVP, a general form of the integral representation in terms of Green's matrix is introduced in Sec. III. This representation is a starting point for the derivation of series expansions and far-field GW asymptotics given in Sec. IV. Those formulas, being a low-cost tool for the analysis of forced GWs, become practically useful with an efficient algorithm for Green's matrix calculation, which is described in Sec. V. The methods of searching for the real and complex roots of the GW characteristic equations, as well as the methods of residue calculation, are generally the same for both isotropic and anisotropic waveguides. Therefore, we skip their description and pass to numerical examples in Sec. VI, where we focus on the manifestation of anisotropy in the directivity of the GWs.

[a]Author to whom correspondence should be addressed. Electronic mail: evg@math.kubsu.ru

II. PROBLEM STATEMENT

Consider a laminate structure subjected to dynamic time-harmonic loading $\mathbf{q}(x,y)e^{-i\omega t}$ applied to a finite area Ω on its top surface (Fig. 1). In Cartesian coordinates $\mathbf{x}=(x,y,z)\equiv(x_1,x_2,x_3)$, the structure occupies the domain $D:|x|<\infty,|y|<\infty,-H\le z\le 0$. It is fabricated from elastic anisotropic sublayers

$$D_m:|x|<\infty,\ |y|<\infty,\ z_{m+1}\le z\le z_m,\quad m=1,2,\ldots,M,$$

$z_1=0,\ z_{M+1}=-H,\ D=\cup_{m=1}^{M}D_m$ (Fig. 1 bottom). The thicknesses of sublayers are $h_m=z_m-z_{m+1}$, while the structure as a whole has thickness $H=\sum_{m=1}^{M}h_m$. The loading causes the elastodynamic response of the structure $\mathbf{u}(\mathbf{x},\omega)e^{-i\omega t}$. Below the harmonic factor $e^{-i\omega t}$ is conventionally omitted and the calculations are carried out with respect to the complex amplitudes of the corresponding values. Transient wave fields $\mathbf{u}(\mathbf{x},t)$ generated by non-harmonic loads can be obtained via the frequency spectrum $\mathbf{u}(\mathbf{x},\omega)$ using fast Fourier transform (FFT) integration in the frequency domain.

The complex amplitudes of the displacement vector $\mathbf{u}$ and of the stress and strain tensors σ_{ij} and ε_{ij} obey the constitutive relations of linear elasticity

$$\sigma_{ij,j}+\rho\omega^2u_i=0,\quad i=1,2,3, \tag{1}$$

$$\sigma_{ij}=C_{ijkl}\varepsilon_{kl},\quad i,j=1,2,3, \tag{2}$$

$$\varepsilon_{kl}=(u_{k,l}+u_{l,k})/2,\qquad k,l=1,2,3. \tag{3}$$

The substitution of Eqs. (2) and (3) into Eq. (1) yields the elastodynamic equations

$$C_{ijkl}u_{l,jk}+\rho\omega^2u_i=0,\quad i=1,2,3. \tag{4}$$

The elastic stiffness tensor C_{ijkl} and the density ρ are piecewise constant functions of the transverse coordinate z, thereby keeping constant values within sublayers D_m. Hereinafter, classical notations in terms of x, y, z components are used together with the tensor ones. The latter assumes summation over identical indices and space derivatives defined by comma, e.g., $\sigma_{ij,j}=\sum_{j=1}^{3}\partial\sigma_{ij}/\partial x_j$. Column vectors are distinguished from row vectors by braces

$$\mathbf{u}=\{u_1,u_2,u_3\}=(u_1,u_2,u_3)^T.$$

The outer sides of the laminate structure $z=0$ and $z=-H$ are stress-free except within the loading region Ω:

$$\boldsymbol{\tau}|_{z=0}=\mathbf{q}\qquad\left(\mathbf{q}(x,y)\equiv 0\text{ for }(x,y)\notin\Omega\right)$$
$$\boldsymbol{\tau}|_{z=-H}=0, \tag{5}$$

and the sublayers are perfectly bonded with each other

$$[\mathbf{u}]_m=0,\quad [\boldsymbol{\tau}]_m=0,\quad m=2,3,\ldots,M. \tag{6}$$

Here, $\boldsymbol{\tau}=\{\tau_{xz},\tau_{yz},\sigma_z\}=\{\sigma_{13},\sigma_{23},\sigma_{33}\}$ is a traction vector at a horizontal surface area $z=\text{const}$. By the brackets $[\cdots]_m$, we denote a jump of a vector-function on the mth interface $z=z_m$

$$[\mathbf{u}]_m=\lim_{\varepsilon\to 0}(\mathbf{u}|_{z=z_m-\varepsilon}-\mathbf{u}|_{z=z_m+\varepsilon}).$$

The technique described below can be easily modified for other types of boundary conditions, e.g., for imperfect interface bonding described by the spring boundary conditions $\boldsymbol{\tau}|_{z=z_m}=B_m[\mathbf{u}]_m,\quad [\boldsymbol{\tau}]_m=0$ instead of Eq. (6). The structure may have a clamped bottom ($\mathbf{u}_{z=-H}=0$) or it may be a layered half-space ($H=\infty$) with a radiation condition as $z\to-\infty$. For definiteness, the general scheme of the method is depicted by the way of problem (4)–(6) for a stress-free composite laminate plate. This problem is typical for GW-based structural health monitoring (SHM).

For the numerical examples below, we have selected two laminate samples A and B of the same total thickness $H=3$ mm but consisting of $M=4$ and $M=8$ sublayers D_m of thickness $h_m=H/M$. The stacking sequences are

$$A:\ [45^\circ,-45^\circ,-45^\circ,45^\circ]\quad\text{and}$$
$$B:\ [45^\circ,0^\circ,-45^\circ,90^\circ,45^\circ,0^\circ,-45^\circ,90^\circ].$$

Sample A is symmetric with respect to the middle plane $z=-H/2$, while laminate B is non-symmetric. The ply material characteristics (AS4/3502 graphite/epoxy) are the same as in Ref. 8

C_{11}	C_{12}	C_{13}	C_{22}	C_{23}	C_{33}	C_{44}	C_{55}	C_{66}	ρ
130.7	5.2	5.2	13.0	4.5	13.0	13.7	6.0	6.0	1578

(7)

$C_{\alpha\beta}$ are in gigapascals (1 GPa $=10^9$ N/m^2), ρ is in kilogram per cubic meter. The stiffness constants C_{ijkl} are expressed via $C_{\alpha\beta}$ in accordance with Voigt's convention

ij or kl :	11	22	33	23	13	12
α or β :	1	2	3	4	5	6

The constants (7) are given for the coordinate system $\mathbf{x}'$ that coincides with the principal material axes. In specific sublayers D_m they do not necessarily coincide with the axes

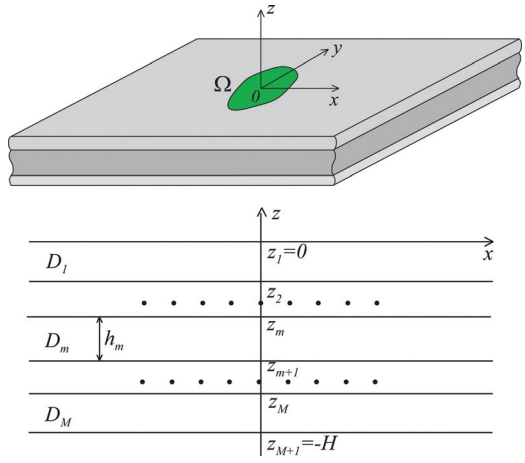

FIG. 1. (Color online) Geometry of the problem.

of the global coordinate system $\mathbf{x}$. Therefore, the values C_{ijkl} entering into governing Eqs. (2) and (4) must be recalculated for every D_m using the 6×6 transformation matrix[12] or just the transform relation

$$C_{ijkl} = p_{mi}p_{nj}p_{rk}p_{sl}C'_{mnrs}$$

where the constants C'_{mnrs} are for the system $\mathbf{x}'$ and p_{ij} are components of the orthogonal rotation matrix P : $\mathbf{x} = P\mathbf{x}'$.

Sample A is the same as specimen I in Ref. 8. The same way as in Ref. 8, we fix dimensionless parameters by taking H as a unit of length, ρ as a unit of density, and the transverse wave velocity $c_T = \sqrt{\mu_{12}/\rho} = 1945$ m/s as a unit of velocity. Then, the dimensionless angular frequency $\omega = 2\pi f H/c_T$, where f is dimensional frequency, and the spatial dimensionless variables are $h_m := h_m/H$, $r := r/H$, $x := x/H$, $\mathbf{u} := \mathbf{u}/H$ and so on. All the results below are given in dimensionless form and the use of the same notations as for the related physical quantities should not be confusing.

As for the wave sources, we confine ourselves to the simplest vertical point load (PL) and to a ring delta-like distribution of surface radial tension (RT)

$$\begin{aligned} &\text{PL:} \quad \mathbf{q} = \delta(x,y)\mathbf{i}_3 \text{ and} \\ &\text{RT:} \quad \mathbf{q} = \{\tau_{rz}\cos\varphi, \tau_{rz}\sin\varphi, 0\}, \ \tau_{rz}|_{z=0} \\ &\qquad = \delta_r(r-a), \end{aligned} \tag{8}$$

where φ is a polar angle in the Oxy plane.

The PL simulates a concentrated normal impact on the surface $z = 0$ (e.g., by a laser beam), while the RT models the action of a circular patch piezo-actuator bonded to the surface in a low frequency range.[13] Such a flexible piezo-patch is designed to stretch and contract in the radial direction generating radial shear contact tension, which is concentrated at the patch border $r = a$. In Eq. (8), such concentrated tension is approximated by the ring delta-function δ_r possessing the property

$$2\pi\int_0^\infty f(r)\delta_r(r-a)rdr = f(a).$$

III. INTEGRAL REPRESENTATION

In the general case, the load $\mathbf{q}$ applied to the surface may be of different nature. It may describe the distribution of contact stresses under an interacting body (indentor, transducer, piezo-patch actuator, and so on) or simulate the effect of laser-generated thermal stresses. For specified $\mathbf{q}$, the numerical evaluation is carried out based on the representation of $\mathbf{u}$ via the convolution of the Green's matrix $k(\mathbf{x},\omega)$ for the structure with the vector-function $\mathbf{q}$:

$$\mathbf{u} = k * \mathbf{q} = \iint_\Omega k(x-\xi, y-\eta, z)\mathbf{q}(\xi,\eta)d\xi d\eta. \tag{9}$$

The frequency-domain Green's matrix $k = (\mathbf{k}_1 \vdots \mathbf{k}_2 \vdots \mathbf{k}_3)$ is formed from the solution vectors $\mathbf{k}_j$ corresponding to concentrated PLs applied along the basic coordinate vectors $\mathbf{i}_j$, $j = 1, 2, 3$. Specifically, in the case under consideration, the columns $\mathbf{k}_j$ are the solutions $\mathbf{u}$ of problem (4)–(6) with the surface boundary conditions $\boldsymbol{\tau}|_{z=0} = \mathbf{i}_j\delta(x,y)$, $j = 1, 2, 3$, respectively. $\delta(x,y)$ is Dirac's delta-function.

Representation (9) may be converted into the Fourier transform domain and rewritten in terms of Fourier symbols. The forward and inverse Fourier transforms $\mathcal{F}_{xy}$ and $\mathcal{F}_{xy}^{-1}$ over horizontal coordinates x and y are used in the form

$$\begin{aligned} \mathcal{F}_{xy}[\mathbf{u}] &= \int_{-\infty}^{\infty}\int_{-\infty}^{\infty}\mathbf{u}(x,y,z)e^{i(\alpha_1 x+\alpha_2 y)}dxdy = \mathbf{U}(\alpha_1,\alpha_2,z), \\ \mathcal{F}_{xy}^{-1}[\mathbf{U}] &= \frac{1}{(2\pi)^2}\int_{\Gamma_1}\int_{\Gamma_2}\mathbf{U}(\alpha_1,\alpha_2,z)e^{-i(\alpha_1 x+\alpha_2 y)}d\alpha_1 d\alpha_2 \\ &= \mathbf{u}(x,y,z). \end{aligned} \tag{10}$$

The integration paths Γ_1 and Γ_2 go along the real axes, deviating from them into the complex planes α_1 and α_2 for rounding real poles of the integrand $\mathbf{U}(\alpha_1,\alpha_2,z)$. The direction of deviation is taken in accordance with the principle of limiting absorption.[14] The contours bypass the poles from the sides opposite to the directions of their shifting off from the real axes when a small attenuating force $-i\varepsilon\omega\mathbf{u}$, $\varepsilon << 1$ proportional to the amplitude of the velocity $\partial/\partial t\,[\mathbf{u}e^{-i\omega t}] = -i\omega\mathbf{u}e^{-i\omega t}$ is introduced into governing equations (4).

In that way

$$\mathbf{u}(\mathbf{x}) = \frac{1}{(2\pi)^2}\int_{\Gamma_1}\int_{\Gamma_2}K(\alpha_1,\alpha_2,z)\mathbf{Q}(\alpha_1,\alpha_2)e^{-i(\alpha_1 x+\alpha_2 y)}d\alpha_1 d\alpha_2, \tag{11}$$

where $K = \mathcal{F}_{xy}[k]$ and $\mathbf{Q} = \mathcal{F}_{xy}[\mathbf{q}]$ are Fourier symbols (transforms) of Green's matrix $k(\mathbf{x})$ and of the load $\mathbf{q}$ (x, y), respectively. A particular form of matrix K (and so of $k(\mathbf{x}) = \mathcal{F}_{xy}^{-1}[K]$) depends on the specific properties of the structure. The forms of $\mathbf{Q}$ for sources (8) are

$$\begin{aligned} &\text{PL:} \quad \mathbf{Q} = \mathbf{i}_3 \quad \text{and} \\ &\text{RT:} \quad \mathbf{Q}(\alpha,\gamma) = \{i\cos\gamma J_1(a\alpha), i\sin\gamma J_1(a\alpha), 0\} \end{aligned} \tag{12},$$

where J_1 is the Bessel function.

If the space variables $\mathbf{x}$ and the Fourier parameters $\alpha = (\alpha_1,\alpha_2,\alpha_3)$ are taken in the cylindrical coordinates (r,φ,z) and (α,γ,α_3)

$$\begin{aligned} &\alpha_1 = \alpha\cos\gamma \quad && x = r\cos\varphi \quad && r = \sqrt{x^2+y^2} \\ &\alpha_2 = \alpha\sin\gamma\,, && y = r\sin\varphi\,, && \alpha = \sqrt{\alpha_1^2+\alpha_2^2}\,, \\ &\alpha_3 = \alpha_3 && z = z && 0 \le \gamma, \varphi \le 2\pi \end{aligned} \tag{13}$$

then the integral representation (11) takes the form

$$\begin{aligned} \mathbf{u}(\mathbf{x}) = \frac{1}{(2\pi)^2}\int_{\Gamma_+}\int_0^{2\pi}K(\alpha,\gamma,z)\mathbf{Q}(\alpha,\gamma) \\ \times e^{-i\alpha r\cos(\gamma-\varphi)}d\gamma\,\alpha d\alpha, \end{aligned} \tag{14}$$

where Γ_+ is an integration contour, going in the complex plane α along the real semi-axis $\mathrm{Re}\,\alpha \ge 0$, $\mathrm{Im}\,\alpha = 0$. As a rule, it bypasses real poles $\zeta_n = \zeta_n(\gamma) > 0$ of the matrix K

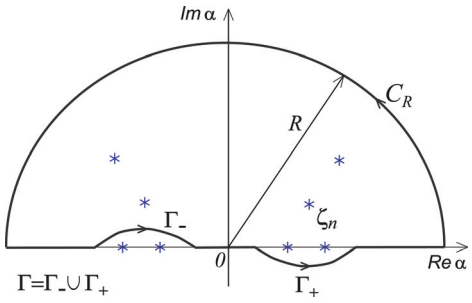

FIG. 2. (Color online) Integration contour Γ_+, whole-axis contour Γ and closing contour C_R.

elements from below (Fig. 2), while infrequent irregular poles associated with so-called backward modes appearing in the ranges enclosed between zero group velocity (ZGV) frequencies[15,16] are rounded from above.

Remark 1. Hereinafter, we use the same notations for functions depending on vector arguments taken in different coordinate systems, e.g., $\mathbf{u}$ (x, y, z) and $\mathbf{u}(r, \varphi, z)$, $\mathbf{Q}(\alpha_1, \alpha_2)$ and $\mathbf{Q}(\alpha, \gamma)$, etc, though one should keep in mind that

$$\mathbf{u}(r, \varphi, z) := \mathbf{u}(r\cos\varphi, r\sin\varphi, z) \quad \text{and}$$
$$\mathbf{Q}(\alpha, \gamma) := \mathbf{Q}(\alpha\cos\gamma, \alpha\sin\gamma)$$

In outward appearance, representations (11) and (14) look the same as those for an isotropic laminate structure; the difference is in more complex dependence of the elements $K_{ij} = \hat{K}_{ij}/\Delta$ of matrix K on the angular variable γ. In an isotropic case γ enters into the numerators $\hat{K}_{ij}(\alpha, \gamma)$ via the factors $e^{\pm im\gamma}$ with the only possible values $m = 0$, 1, and 2, while the denominator $\Delta(\alpha)$ and, consequently, the poles ζ_n are independent of γ. In an anisotropic case, $\hat{K}_{ij}(\alpha, \gamma)$ and $\Delta(\alpha, \gamma)$ are smooth functions of γ and, correspondingly, the poles ζ_n obtained from the characteristic equation $\Delta(\alpha, \gamma) = 0$ are also functions of γ.

This difference is not vital for direct numerical integration over the paths Γ_1, Γ_2, or Γ_+, which is implemented the same way as in the isotropic case (e.g., Ref. 17 and the references cited therein). Hence, with given K and $\mathbf{Q}$ integral representations (11) and (14) may effectively be used for numerical evaluation of the composite plate dynamic response $\mathbf{u}(\mathbf{x})$ in a not distant vicinity of the area of loading Ω. However, with increasing distance from Ω, direct numerical integration becomes too time consuming due to the oscillating factor $e^{-i(\alpha_1 x+\alpha_2 y)}$ in the integrand. This restriction is conventionally overcome via the use of GW asymptotics derived in terms of residues from the poles ζ_n.

IV. GUIDED WAVES

Within a 2D statement, when $\mathbf{q}$ and $\mathbf{u}$ are independent of one horizontal space variable (e.g., of y), only a one-fold integration over Γ_1 remains in representation (11). Therefore, the contribution of residues is easily derived via closing the integration path Γ_1 into the upper or lower half-plane of the complex plane $\alpha = \alpha_1$ in accordance with the Jordan lemma. Then, in accordance with the Cauchy residue theorem, the original path integral is equal to the sum of the residues from the poles inside the closed contour. Unfortunately, in a 3D statement, the double integrals of form (11) or (14) cannot be processed in the same way. If one integration (say over Γ_1) is replaced by the sum of residues, the integration over Γ_2 is still required. Such an approach, combining the residue technique with the numerical integration is also implemented,[18] but it remains rather time consuming. To a considerable degree, this is because the poles and residues with respect to α_1 are functions of α_2 and so must be recalculated at every step of numerical integration over Γ_2. That is why in many cases (e.g., Refs. 11 and 19) 3D GW asymptotics are constructed as a superposition of 2D asymptotic solutions.

Integrals of form (14) cannot be directly reduced to a sum of residues since the path Γ_+ does not go along the whole real axis $-\infty < \mathrm{Re}\,\alpha < \infty$, $\mathrm{Im}\,\alpha = 0$. Its closing adds an integration over a contour coming back from infinity to the origin $\alpha = 0$, which remains as an addition to the residues. This obstacle can be avoided by means of the so-called contour centerfold procedure for the Γ_+ central spreading onto the whole-axis contour $\Gamma = \Gamma_+ \cup \Gamma_-$ (Fig. 2). For the Green matrix,

$$k(\mathbf{x}) = \frac{1}{(2\pi)^2}\int_{\Gamma_+}\int_0^{2\pi} K(\alpha, \gamma, z)e^{-i\alpha r\cos(\gamma-\varphi)}d\gamma\alpha d\alpha, \qquad (15)$$

this procedure is accomplished based on the series representation[20]

$$e^{-i\alpha r\cos(\gamma-\varphi)} = \sum_{m=-\infty}^{\infty} J_m(\alpha r)e^{im(\gamma-\varphi-\pi/2)} \qquad (16)$$

and the splitting property

$$J_m(z) = \frac{1}{2}\left[H_m^{(1)}(z) + H_m^{(2)}(z)\right],$$

where J_m and $H_m^{(1,2)}$ are the Bessel and Hankel functions. The change of variable $\alpha := -\alpha$ in the integrals with $H_m^{(2)}$ converts them into the integrals over the supplemented path Γ_- (Fig. 2), while the properties

$$H_m^{(2)}(-\alpha r) = (-1)^{m+1}H_m^{(1)}(\alpha r) \quad \text{and}$$
$$K(-\alpha, \gamma) = K(\alpha, \gamma + \pi) \qquad (17)$$

finally lead to the same integrands as in the integrals over Γ_+. Ultimately, we arrive at the representation

$$k(\mathbf{x}) = \frac{1}{8\pi^2}\sum_{m=-\infty}^{\infty}\int_0^{2\pi}\int_{\Gamma} K(\alpha, \gamma, z)H_m^{(1)}(\alpha r)\alpha d\alpha \times e^{im(\gamma-\varphi-\pi/2)}d\gamma, \qquad (18)$$

in which Γ can be closed upward by a semicircle contour C_R of a large radius R (Fig. 2) due to the integrands' exponential decrease assured by the Hankel function behavior

$$H_m^{(1)}(\alpha r) = (-i)^m\sqrt{2/(i\pi\alpha r)}e^{i\alpha r}[1 + O(|\alpha r|^{-1})], \quad |\alpha r| \to \infty. \qquad (19)$$

The residue theorem brings Eq. (18) to the double series representation

$$k(\mathbf{x}) = \sum_{n=1}^{\infty} k_n(\mathbf{x}), \quad k_n(\mathbf{x}) = \sum_{m=-\infty}^{\infty} k_{nm}(r,z)e^{-im(\varphi+\pi/2)}$$
$$k_{nm} = \frac{1}{2\pi}\int_0^{2\pi} R_n(\gamma,z)H_m^{(1)}(\zeta_n r)e^{im\gamma}d\gamma, \tag{20}$$
$$R_n(\gamma,z) = \frac{i}{2}j_n\zeta_n \mathrm{res}K(\alpha,\gamma,z)|_{\alpha=\zeta_n},$$

where nearly always $j_n = 1$, except in the case of infrequent irregular real poles yielding backward modes for which $j_n = -1$. Poles $\zeta_n(\gamma)$ falling inside the closed contour lie in the upper half-plane $\mathrm{Im}\,\alpha \geq 0$ above the contour Γ. They are numbered in ascending order with respect to $\mathrm{Im}\,\zeta_n$ increasing ($\mathrm{Im}\,\zeta_{n+1} \geq \mathrm{Im}\,\zeta_n$) so that the real ones arise first.

With a fixed order m, the terms k_{nm} exponentially decay as n increases in accordance with asymptotics (19)

$$k_{nm}(r,z) \sim O(e^{-\mathrm{Im}\,\zeta_n r}), \quad n \to \infty, \quad \mathrm{Im}\,\zeta_n r \to \infty. \tag{21}$$

Therefore, only a limited number of poles ζ_n and residues R_n are needed for a practical $k(\mathbf{x})$ approximation by a truncated sum (20)

$$k(\mathbf{x}) \approx \sum_{n=1}^{N} k_n(\mathbf{x}), \quad N \geq N_r. \tag{22}$$

The number of kept terms N is inversely proportional to r but should be no less than the number of real poles N_r.

Moreover, with respect to m, the terms k_{nm} also tend to zero faster than any power

$$\lim_{m\to\infty} k_{nm}m^p = 0 \quad \text{for any } p,$$

because they are in fact the Fourier-series coefficients of infinitesimally smooth functions of γ [see Eq. (20)]. Thus, the series for $k_n(\mathbf{x})$ can also be truncated with high accuracy.

In the special case of isotropic materials, the series representing k_n exactly degenerates to the finite sum

$$k_n(\mathbf{x}) = \sum_{m=-2}^{2} k_{nm}(r,z)e^{-im(\varphi+\pi/2)} \tag{23}$$

in view of the above mentioned K-matrix expansion

$$K(\alpha,\gamma,z) = \sum_{m=-2}^{2} K_m(\alpha,z)e^{im\gamma} \tag{24}$$

and the poles' independence of γ. In this case,

$$k_{nm}(r,z) = R_{nm}(z)H_m^{(1)}(\zeta_n r),$$
$$R_{nm} = \frac{i}{2}j_n\zeta_n \mathrm{res}\,K_m(\alpha,z)|_{\alpha=\zeta_n},$$

and Eq. (23), in fact, provides an exact analytical representation for normal modes excited in an isotropic laminate by PLs $\delta(x,y)\mathbf{i}_j$. The substitution of asymptotics (19) into sum (23) yields the far-field asymptotics of Green's matrix $k(\mathbf{x})$ for the isotropic case

$$k(\mathbf{x}) = \sum_{n=1}^{N_r} b_n(\varphi,z)e^{i\zeta_n r}/\sqrt{\zeta_n r}[1+O((\zeta_n r)^{-1})], \zeta_n r \to \infty$$
$$b_n = \sqrt{\frac{i}{2\pi}}\zeta_n \mathrm{res}K(-\alpha,\varphi,z)|_{\alpha=\zeta_n}. \tag{25}$$

The terms of this expansion are cylindrical GWs propagating in radial directions with the phase velocity $v_n = \omega/\zeta_n$. Their amplitude functions b_n coincide within constant factors to the cross-sectional eigenforms obtained via the modal analysis technique.

In the anisotropic case, however, the pole variation $\zeta_n(\gamma)$ prevents drawing the Hankel functions out of the integrals over γ. Therefore, although every term $k_n(\mathbf{x})$ may be still treated as a GW associated with the pole ζ_n, their far-field asymptotics is derived directly from Eq. (15) without resort to expansion (16).

Unfortunately, the central spreading into the contour Γ with respect to the same integrand on the Γ_- and Γ_+ parts is not possible here. Instead, Eq. (15) may be brought to the form

$$k(\mathbf{x}) = \frac{1}{(2\pi)^2}\left(\int_{\Gamma_+} - \int_{\Gamma_-}\right)\int_0^{\pi} K(\alpha, \beta+\varphi+\pi/2, z) \times e^{iz r\sin\beta}d\beta\alpha d\alpha.$$

It is derived by the change of variables

$$\gamma = \beta+\varphi-\pi/2 \quad \text{for} \quad -\pi/2 < \gamma-\varphi < \pi/2 \quad \text{and}$$
$$\gamma = \beta+\varphi+\pi/2 \quad \text{for} \quad \pi/2 < \gamma-\varphi < 3\pi/2$$

accompanied by the change $\alpha := -\alpha$ and the use of property (17) in the first case. Both path integrals can be closed upward with the same backward integration over the imaginary semi-axis $\alpha = i\tau$, $0 \leq \tau < \infty$. The residue theorem brings them to the form

$$k(\mathbf{x}) = \sum_{n=1}^{N_r} k_n(\mathbf{x}) + k_c(\mathbf{x}),$$
$$k_n = \frac{1}{\pi}\int_0^{\pi} R_n(\theta,z)e^{is_n(\beta)r}d\beta, \quad s_n(\beta) = \zeta_n(\theta)\sin\beta,$$
$$\theta = \beta+\varphi+\pi/2,$$
$$k_c(\mathbf{x}) = \sum_{n=N_r+1}^{\infty} \mathrm{sign}(\mathrm{Re}\,\zeta_n)k_n(\mathbf{x}) - \frac{1}{2\pi^2}\int_0^{\infty}\int_0^{\pi} K(i\tau,\theta,z)e^{-r\tau\sin\beta}d\beta\tau d\tau, \tag{26}$$

where R_n are the same residues as in Eq. (20), but with the angular argument θ shifted. The terms k_n in the first sum are associated with the real poles ζ_n, while the sum over complex poles ($n > N_r$) enters into k_c together with the integral over the imaginary semi-axis remaining from the closed contour. Since the terms associated with complex poles exhibit exponential decrease (21), a far-field behavior of k_c is determined by that integral. A rough asymptotic estimation shows that if $\zeta r \to \infty$, where ζ is a

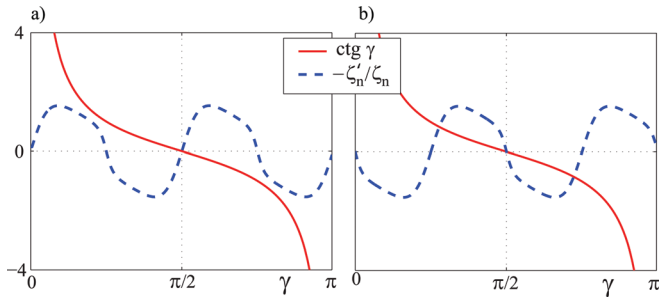

FIG. 3. (Color online) Single intersection of the ctg γ and $-\zeta_n'/\zeta_n$ curves yielding one stationary point $\gamma_1 \approx \pi/2$ for $\varphi = 45°$ (a) and multiple intersections for $\varphi = 0°$ (b); sample A, $\omega = 1$, $n = 2$, SH mode.

characteristic wave number, it goes down at least as $O((\zeta r)^{-1})$. This is faster than the decrease of residue terms k_n exhibiting with real ζ_n the square-root behavior $O((\zeta r)^{-1/2})$. The latter follows from the stationary phase asymptotics for the integrals over β

$$k_n(\mathbf{x}) = \sum_{m=1}^{M_n} b_{nm}(\varphi, z) e^{is_{nm}r}/\sqrt{\zeta r}\,[1 + O((\zeta r)^{-1})],\ r \to \infty$$
$$b_{nm} = \sqrt{2i\zeta/(\pi s_n''(\gamma_m))}R_n(\theta_m, z), \tag{27}$$
$$s_{nm} = s_n(\gamma_m), \theta_m = \gamma_m + \varphi + \pi/2.$$

Here γ_m are stationary points, i.e., the roots of equation $s_n'(\gamma) = 0$, which has the form $\mathrm{ctg}\,\gamma = -\zeta_n'(\theta)/\zeta_n(\theta)$. M_n is the number of roots γ_m in the interval of integration $0 < \gamma < \pi$.

In the isotropic case $\zeta_n' \equiv 0$ and the only stationary point, $\gamma_1 = \pi/2$ yields the far-field asymptotics coinciding with Eq. (25). In the anisotropic case, the cotangent curve also intersects the curve ζ_n'/ζ_n at least once, yielding the root γ_1 located near $\pi/2$ [Fig. 3(a)]. In addition, for certain directions φ multiple intersections of these curves may also occur [Fig. 3(b)] resulting in several roots γ_m, i.e., in $M_n > 1$ cylindrical GWs propagating in φ direction with the phase velocities $v_{nm} = \omega/s_{nm}$. In this context, the values $s_{nm} = \zeta_n(\theta_m)\sin\gamma_m$ are nothing but the wave numbers of cylindrical modes (27), which reduce to the conventional wave numbers ζ_n in the isotropic case.

With an anisotropic sample, the phase velocities of cylindrical modes $v_n^c(\varphi) = \omega/s_n(\varphi)$ may considerably differ from the phase velocities $v_n^p(\varphi) = \omega/\zeta_n(\varphi)$ introduced for plane waves.[12] Due to the occurrence of several roots γ_m, the angular diagrams for the $v_n^c(\varphi)$ may have self-crossing loops [Fig. 4(b)], while the plane-wave diagrams $v_n^p(\varphi)$ are always without such loops [Fig. 4(a)]. The test examples of Fig. 4 are for the reference input parameters, therefore, the curves $v_n^p(\varphi)$ of Fig. 4(a) coincide with those shown in Figs. 5(a) and 5(d) from Ref. 8. As for the loops in Fig. 4(b), they take place for the same modes (SH_0 and SH_1) as those observed for the wave curves in Figs. 5(c) and 5(f) from Ref. 8. However, those diagrams have different physical interpretation, because $v_n^c(\varphi)$ are characteristics of cylindrical GWs (27), while the wave curves[8] are associated with group velocities of plane waves going in various directions φ.

The far-field asymptotics for GWs generated by a load $\mathbf{q}$ is easily derived from convolution (9) by the substitution $k(\mathbf{x})$ in form (27) and subsequent cubature discretization of the integration over Ω

$$\mathbf{u}(\mathbf{x}) = \sum_{n=1}^{N} \mathbf{u}_n(\mathbf{x}) + O((\zeta r)^{-1}), \quad \zeta r \to \infty,$$
$$\mathbf{u}_n(\mathbf{x}) = h^2 \sum_{j=1}^{N_j} \sum_{m=1}^{M_{nj}} b_{nm}(\varphi_j, z)\mathbf{q}_j e^{is_{nmj}r_j}/\sqrt{\zeta r_j}. \tag{28}$$

Here $\mathbf{q}_j = \mathbf{q}(x_j, y_j)$, (x_j, y_j) are cubature nodes covering Ω with a spacing h, $r_j = \sqrt{(x - x_j)^2 + (y - y_j)^2}$ and φ_j : $\cos\varphi_j = (x - x_j)/r_j$, $\sin\varphi_j = (y - y_j)/r_j$. The stationary phase equations must be solved for every direction φ_j yielding in M_{nj} roots γ_{mj}; $s_{nmj} = s_n(\gamma_{mj})$.

The terms $\mathbf{u}_n$ are superpositions of cylindrical GWs generated by elementary sources located at the nodes $\mathbf{x}_j = (x_j, y_j, 0)$. They propagate with phase velocities which are approximately equal to those associated with the direction φ. At sufficiently large distances, such that all the directions φ_j become practically parallel each other ($\varphi_j \approx \varphi$), one can use the estimation

$$r_j \sim r - (x_j\cos\varphi + y_j\sin\varphi) + O(|\mathbf{x}_j|/r), r \to \infty \tag{29}$$

to change the sum over j into the integral sum for $\mathbf{Q} = \mathcal{F}_{xy}[\mathbf{q}]$ at $\alpha_1 = -s_{nm}\cos\varphi$ and $\alpha_2 = -s_{nm}\sin\varphi$. It leads to the more compact asymptotic representation

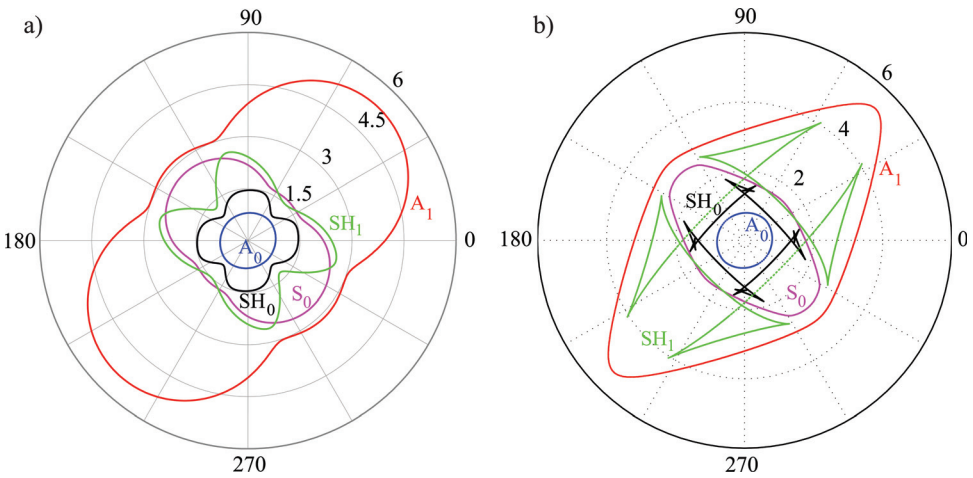

FIG. 4. (Color online) Angular diagrams for the phase velocities of plane (a) and cylindrical (b) modes, sample A, $\omega = 1$.

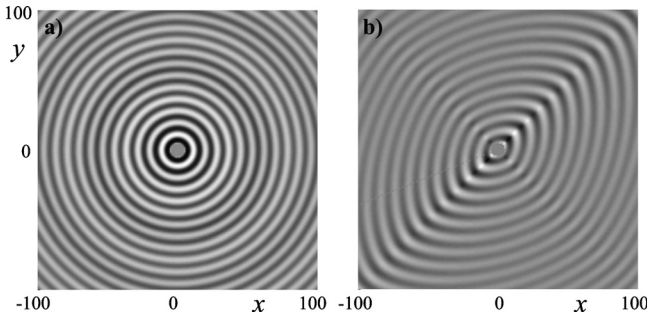

FIG. 5. Out-of-plane displacements $\mathrm{Re}\, u_z(x, y, 0)$ generated by a circular piezo-patch in an isotropic plate (a) and in laminate A (b) by the RT source of radius $a = 5$ at $\omega = 0.25$.

$$\mathbf{u}_n(\mathbf{x}) \sim \sum_{m=1}^{M_n} \mathbf{a}_{nm}(\varphi, z) e^{is_{nm}r}/\sqrt{\zeta r}, \quad \zeta r \to \infty$$
$$\mathbf{a}_{nm} = b_{nm}(\varphi, z)\mathbf{Q}(-s_{nm}, \varphi), \tag{30}$$

which is valid when condition (29) holds. It is especially convenient when an analytical form of $\mathbf{Q}(\alpha, \gamma)$ is available.

Thus, double-integral representation (14), residue series (20) with one-dimensional angular integration and closed-form asymptotics (27)–(30) provide three different ways to calculate the wave field. They are advantageous in overlapping near-field, intermediate and far-field zones, respectively. The upper limit r_0 of the near-field range $0 \le r < r_0$ is conditioned by computational costs, increasing in parallel with r due to the oscillation of the exponential factor in the integrand, while the lower limit r_- of the intermediate zone $r_- \le r \le r_+$ depends on the number of terms kept in truncated series (20) (the larger the number of complex poles ζ_n and terms in sums over m are accounted for, the smaller r_- can be taken, down to $r_- = 0$ for the infinite series). The usage of residue expansions has to be supplemented with a prior tabulation of the poles $\zeta_n(\gamma)$ and residues $R_n(\gamma)$, preventing repeated recalculations for different r. Hence, the upper limit r_+ depends on the accuracy of numerical integration over γ with the tabulated values entering into the integrands for k_{nm}. The lower limit r_a of the far-field distances $r_a < r < \infty$ is controlled by the accuracy of stationary phase asymptotics (27) and by the error induced by neglecting the term k_c. Test computations show that the latter contribution is much smaller than might be expected from the rough estimation $k_c \sim O((\zeta r)^{-1})$, as $\zeta r \to \infty$. With asymptotics (27), (28), and (30), no integration and no pole tabulation is needed. Therefore, they are ideal for a fast GW analysis, in particular, for depicting angular diagrams for waves radiated from a given source to infinity.

V. GREEN'S MATRIX CALCULATION

The application of the integral and asymptotic representations derived above assumes the use of effective algorithms for the matrix K calculation. The algorithm described below has been elaborated as a generalization of the methods developed for isotropic multilayered and functionally gradient waveguides,[21,22] being in the category of transfer matrix algorithms. The crucial point here is ensuring numerical stability over the entire range of input parameters. In addition to standard techniques preventing the occurrence of exponential factors in the diagonal blocks,[10,21,23] we also use a scheme preventing ill-conditioned matrix inversions in the course of recursive calculations.

In the isotropic case, the transform $\mathcal{F}_{xy}$ converts the Lamé equations into a system of linear ordinary z-differential equations (ODEs) with respect to $\mathbf{U}(\alpha_1, \alpha_2, z)$. Their general solution with several unknown coefficients can be written in a closed analytical form. The substitution of such solutions, derived for every sublayer D_m, into the interface and external boundary conditions leads to linear matrix equations with respect to the unknown coefficients. These equations are solved by means of recursive matrix algorithms.

The execution of this scheme with anisotropic materials encounters certain obstacles. First, the transform $\mathcal{F}_{x_1x_2}$ being applied to Eq. (4) breaks its compactness. The form of the resulting ODEs becomes unwieldy and the general solution cannot be derived analytically in all cases. To avoid this obstacle, we apply the triple transform $\mathcal{F}_{\mathbf{x}}$ with respect to all space variables x_i, $i = 1, 2, 3$, instead of the double transform $\mathcal{F}_{x_1x_2}$. In doing so, the multiplier $-i\alpha_3$ is treated as an operator notation for the derivative $\partial/\partial z$, in accordance with the transform property

$$\mathcal{F}_{\mathbf{x}}\left[\frac{\partial^n \mathbf{u}}{\partial x_j^n}\right] = (-i\alpha_j)^n \mathbf{U}(\alpha), \quad \text{where}$$
$$\mathbf{U}(\alpha) = \mathcal{F}_{\mathbf{x}}[\mathbf{u}], \ \alpha = (\alpha_1, \alpha_2, \alpha_3).$$

As a consequence, the homogeneous ODEs following from Eq. (4) can be written in the form

$$[B(\alpha) - \rho\omega^2 I]\,\mathbf{U}(\alpha_1, \alpha_2, z) = 0, \tag{31}$$

where I is the unitary matrix and $B = [b_{ij}]_{i,j=1}^3$, $b_{ij} = C_{iljk}\alpha_k\alpha_l$ is a matrix form of the Christoffel tensor for anisotropic elastic continuum.[12]

Non-zero solutions to Eq. (31) are sought for in the form $\mathbf{U} = \mathbf{m}e^{\lambda z}$. Its substitution leads to the matrix eigenproblem

$$[B(\alpha) - \rho\omega^2 I]\mathbf{m} = 0 \tag{32}$$

in which $\alpha_3 = i\lambda$. The characteristic equation

$$\det[B(\alpha) - \rho\omega^2 I] = 0 \tag{33}$$

is a polynomial of degree 6 with respect to α_3, hence six eigenvalues $\lambda_n = -i\alpha_{3,n}(\alpha_1, \alpha_2, \omega)$ are expressed via its roots $\alpha_{3,n}$. If all the roots λ_n are single or the number of eigenvectors $\mathbf{m}_n$ associated with multiple roots is equal to the total roots' multiplicity (the Jordan basis does not include adjoint vectors), then the general solution has the form

$$\mathbf{U}(\alpha_1, \alpha_2, z) = \sum_{n=1}^{6} t^{(n)}\mathbf{m}_n e^{\lambda_n z}. \tag{34}$$

Fortunately, a set of input parameters $\alpha_1, \alpha_2, \omega$, for which the Jordan basis contains adjoint vectors and this form becomes

inapplicable, is of measure null. Therefore, such a case is unstable and may be avoided with a minimal variation of parameters. The only important special case, when Jordan blocks of size more than one exist in the whole range of α_1, α_2 variation, is $\omega = 0$, i.e., a static solution. Nevertheless, with a minimal variation of ω the form (34) again becomes applicable for practically all values of α_1 and α_2.

Remark 2. Within the classical Stroh formalism,[24] the matrix of the characteristic equation is expanded in powers λ^k, $k = 0,\ 1,\ 2$. Such an expansion is helpful for analytical calculations, but it is unnecessary for computer root finding directly from Eq. (33).

The roots λ_n may be divided into two groups: $\lambda_j = \sigma_j$ and $\lambda_{j+3} = -\sigma_j$ $(j = 1, 2, 3)$ and arranged as follows:

$$\begin{aligned} &\operatorname{Re}\sigma_1 \geq \operatorname{Re}\sigma_2 \geq \operatorname{Re}\sigma_3 \geq 0 \quad \text{and} \\ &\operatorname{Im}\sigma_3 \leq \operatorname{Im}\sigma_2 \leq \operatorname{Im}\sigma_1 \leq 0. \end{aligned} \tag{35}$$

In the special case of isotropic materials, the roots take the form $\sigma_j = \sqrt{\alpha^2 - \kappa_j^2}$ $(\sigma_3 \equiv \sigma_2)$, where $\alpha^2 = \alpha_1^2 + \alpha_2^2$, $\kappa_j = \omega/v_j$ are the wave numbers of longitudinal P $(j = 1)$ and shear S $(j = 2)$ waves, and v_j are the corresponding phase velocities.

For half-space structures $(H = \infty)$, such root regulation is significant for the rejection of unphysical terms with the exponentials $e^{-i\sigma_j z}$ in Eq. (34) not meeting the attenuation and radiation conditions at infinity $z \to -\infty$. In the sublayers D_m root selection allows one to avoid growing exponentials in the calculations by taking general solutions of the form

$$\begin{aligned} &\mathbf{U} \equiv \mathbf{U}_m = \sum_{j=1}^{3} [t_m^{(j)} \mathbf{m}_j e^{\sigma_j (z - z_m)} + t_m^{(j+3)} \mathbf{m}_{j+3} e^{-\sigma_j (z - z_{m+1})}], \\ &z \in D_m, m = 1, 2, \ldots, M \end{aligned} \tag{36}$$

instead of form (34) (following Ref. 23, a similar form has been used in Ref. 10).

The vectors $\mathbf{U}_m$, as well as the Fourier symbols of the stress vectors $\mathbf{T}_m = \mathcal{F}_{xy}[\tau_m]$, can be written in the compact matrix form

$$\mathbf{U}_m(z) = M_m E_m(z) \mathbf{t}_m, \quad \mathbf{T}_m = -iP_m M_m E_m(z) \mathbf{t}_m, \tag{37}$$

where

$$M_m = [\mathbf{m}_1\ \mathbf{m}_2 \ldots \mathbf{m}_6], \quad P_m = [p_{ij}]_{i,j=1}^{6}, \quad p_{ij} = C_{i3jn}\alpha_n,$$

$$E_m(z) = \operatorname{diag}[e_{m,1}^{+}, e_{m,2}^{+}, e_{m,3}^{+}, e_{m,1}^{-}, e_{m,2}^{-}, e_{m,3}^{-}],$$

$$e_{m,j}^{+} = e^{\sigma_j (z - z_m)}, \quad e_{m,j}^{-} = e^{-\sigma_j (z - z_{m+1})},$$

$$\mathbf{t}_m = \{t_m^{(1)}, t_m^{(2)}, \ldots, t_m^{(6)}\},\ i, j = 1, 2, 3;\ m = 1, 2, \ldots, M.$$

The unknown coefficients $t_m^{(j)}$ assembled into the column vector $\mathbf{t} = \{\mathbf{t}_1, \mathbf{t}_2, \ldots, \mathbf{t}_M\}$ of length $6M$ are obtained from the linear algebraic system

$$A\,\mathbf{t} = \mathbf{f}, \quad \mathbf{f} = \{\mathbf{f}_1, 0, \ldots, 0\},\ \mathbf{f}_1 = \{\mathbf{Q}, 0, 0, 0\}, \tag{38}$$

which follows from the substitution of expressions (36) into the transformed boundary conditions (5) and (6). Outwardly, the matrix A has the same two-diagonal block structure as with isotropic sublayers[22]

$$A = \begin{bmatrix} S_1^{+} & 0 & 0 & \ldots & 0 & 0 \\ C_1^{-} & -C_2^{+} & 0 & \ldots & 0 & 0 \\ 0 & C_2^{-} & -C_3^{+} & \ldots & 0 & 0 \\ \ldots & \ldots & \ldots & \ldots & \ldots & \ldots \\ 0 & 0 & 0 & \ldots & C_{M-1}^{-} & -C_M^{+} \\ 0 & 0 & 0 & \ldots & 0 & S_M^{-} \end{bmatrix} \tag{39}$$

but the size and appearance of the blocks are obviously different

$$C_m^{\pm} = \begin{bmatrix} S_m^{\pm} \\ M_m^{\pm} \end{bmatrix}, \quad S_m^{\pm} = -iP_m M_m^{\pm}, \quad M_m^{\pm} = M_m E_m^{\pm},$$

$$E_m^{+} = E_m(z_m) = \operatorname{diag}[1, 1, 1, e_m^{(1)}, e_m^{(2)}, e_m^{(3)}],$$

$$E_m^{-} = E_m(z_{m+1}) = \operatorname{diag}[e_m^{(1)}, e_m^{(2)}, e_m^{(3)}, 1, 1, 1],$$

$$e_m^{(j)} = e^{-\sigma_j h_m}, \quad h_m = z_m - z_{m+1}.$$

The blocks $C_m^{\pm}$ and $E_m^{\pm}$ are of size 6×6 while $S_m^{\pm}$ and $M_m^{\pm}$ are of size 3×6. The subscript m indicates that the corresponding blocks are expressed via the eigenvalues σ_j, eigenvectors $\mathbf{m}_n$ and elastic stiffness constants C_{ijkl} for the mth sublayer D_m.

Due to the use of representation (36), the diagonal and adjacent to the diagonal elements a_{ij} of matrix A have no exponential factors, while all other non-zero elements may only have the exponentially decreasing factors $e_m^{(j)}$. Correspondingly, A is a well-conditioned matrix and numerical solution of system (38) is stable. With a large number of layers M, the matrix A becomes too large and sparse for the use of direct methods elaborated for dense matrices. The equalities

$$C_m^{-}\mathbf{t}_m = C_{m+1}^{+}\mathbf{t}_{m+1}, \quad m = 1, 2, \ldots, M - 1$$

associated with interface conditions (6) allow one to organize a low-cost recurrent double-sweep algorithm.

Such an approach seems to be quite natural; it is implemented in most transfer matrix algorithms. It fails, however, in some situations. The imperfection results from the degeneration of matrices C_m^{-} into singular ones, due to the exponential decrease of their first three columns with the increase of the parameters αh_m, which control the powers of the exponentials $e_m^{(j)} = e^{-\sigma_j h_m}$.

A stable recurrent algorithm free of this imperfection can be derived by formally subdividing A into 6×6 blocks $A_{mn} : A = [A_{mn}]_{m,n=1}^{M}$. The diagonal blocks A_{mm} remain non-singular as $e_m^{(j)} \to 0$. Moreover, their condition numbers do not become worse after adding neighboring blocks to them. Therefore, a stable recursive process without inversion of ill-conditioned matrices can be organized in the following way

$$
\begin{aligned}
&m = M: \quad B_{M-1} = -A_{MM}^{-1} A_{MM-1},\\
&m = M-1, M-2, \ldots, 2:\\
&B_{m-1} = -(A_{mm} + A_{mm+1} B_m)^{-1} A_{mm-1},\\
&m = 1: \quad B = A_{11} + A_{12} B_1, \qquad \mathbf{t}_1 = B^{-1}\mathbf{f}_1,\\
&m = 2, 3, \ldots, M: \quad \mathbf{t}_m = B_{m-1}\mathbf{t}_{m-1}.
\end{aligned} \tag{40}
$$

Finally, the matrix $K(\alpha_1, \alpha_2, z)$ is constructed based on the solution (36). Its columns $\mathbf{K}_n$ have the same appearance as the vector $\mathbf{U}$ with coefficients $t_m^{(j)}$ found from system (38) for the three right-hand side vectors $\mathbf{f}_1 = \{\mathbf{i}_n, 0, 0, 0\}$, $n = 1, 2, 3$, respectively.

Remark 3. Similar algorithms can be used for the calculation of Green's matrices associated with internal point sources modeled by δ-like jumps of stress or displacement fields: $[\boldsymbol{\tau}]_{m_0} = \delta(x, y)\mathbf{i}_n$ or $[\mathbf{u}]_{m_0} = \delta(x, y)\mathbf{i}_n$ ($n = 1, 2, 3$). Systems (38) formed for such problems differ only by right-hand sides $\mathbf{f}$ containing unit vectors $\mathbf{i}_n$ at the place corresponding to the m_0 block level in the matrix A. Such Green's matrices may be used as special laminate elements (LEs) for the approximation of diffracted wave fields or for the elastodynamic analysis of long but finite laminate structures, as has been accomplished in the isotropic case.[22]

VI. NUMERICAL EXAMPLES

A. GW directivity

Both sources (8) are axially symmetric, therefore, the spatial directivity of the waves may appear to be due only to anisotropy of the material. As an example, Fig. 5 displays the amplitude of the vertical (out-of-plane) displacement $\mathrm{Re}\, u_z(x, y, 0)$ generated by a ring source of radius $a = 5$ in a homogeneous isotropic plate [Fig. 5(a)] and in laminate A [Fig. 5(b)] at $\omega = 0.25$, when the dimensionless transverse wavelength $\lambda_T = c_T/(fH) \approx 25$. The dimensionless properties of the isotropic layer are the same as those of laminate A in the fiber direction: Poisson's ratio $\nu = \nu_{12} = 0.3$, the shear modulus $\mu = \mu_{12} = 1$, and $\rho = 1$. Besides the GW directivity, Fig. 5(b) illustrates the usage of representations (14), (22), and (28) for near-, intermediate-, and far-field ranges. Test computations have shown that for $r > 10$ ($r/\lambda_T > 0.4$), the approximation (22) with the real poles only ($N = N_r = 3$) yields practically the same result as direct numerical integration (14) (i.e., $r_- = 10$). The asymptotics (28) coincides with both of those results for $r > 20$ ($r/\lambda_T > 0.8$, $r_a = 20$). Thus, low-cost asymptotics (28) is applicable even at less than one wavelength distances from the source ($r_a = 0.8\lambda_T$).

More visually than in Fig. 5, the directivity is depicted by angular diagrams based on equations

$$
V_z(\varphi) = \omega |u_z(r, \varphi, 0)| \sqrt{r} \quad \text{and}
$$
$$
E(\varphi) = \int_{-H}^{0} e_r(r, \varphi, z)\, dz, \quad \zeta r >> 1, \quad 0 \le \varphi \le 2\pi \tag{41}
$$

obtained by using the asymptotics (30). Here $e_r = -\frac{\omega}{2}\mathrm{Im}\,(\mathbf{u}, \boldsymbol{\tau}_r)$ is the radial component of the time-averaged power density vector $\mathbf{e}$ (Umov's vector[25]), which specifies the structure of elastic wave energy fluxes in a harmonic field $\mathbf{u}e^{-i\omega t}$; $\boldsymbol{\tau}_r$ is a stress vector at an area element with the radial normal $\mathbf{n} = \{\cos\varphi, \sin\varphi, 0\}$. The characteristic $V_z(\varphi)$ describes the far-field angular distribution of the amplitude of the out-of-plane particle velocity at the surface, while $E(\varphi)$ yields the total (integrated over the vertical cross-section) amount of wave energy propagating from the source to infinity in the direction φ. As in the case of isotropic waveguides,[17] the wave energy fluxes can be visualized by energy streamlines tangential to the vector field $\mathbf{e}$ ($\mathbf{x}$).

Figure 6 shows examples of $V_z(\varphi)$ diagrams for GWs excited by both sources (8) in the laminate A at the frequencies $\omega = 0.25$, 1 and 1.75. Hereinafter, $a = 5$ if not specified otherwise. Similar diagrams for the 8-layer substrate B are presented in Fig. 7. One can see that with both specimens the directivity of surface waves generated by the point source is practically independent of frequency [Figs. 6(a) and 7(a)], whereas the directivity of the sized RT source is frequency dependent. With plate A at $\omega = 0.25$ the main lobe is directed along the fibers of upper plies ($\varphi = 45°$), but at $\omega = 1$ and $\omega = 1.75$ it turns to the fiber direction of inner sublayers ($\varphi = 135°$) [Fig. 6(b)]. With structure B this dependence is even more complex [Fig. 7(b)], while the PL yields just

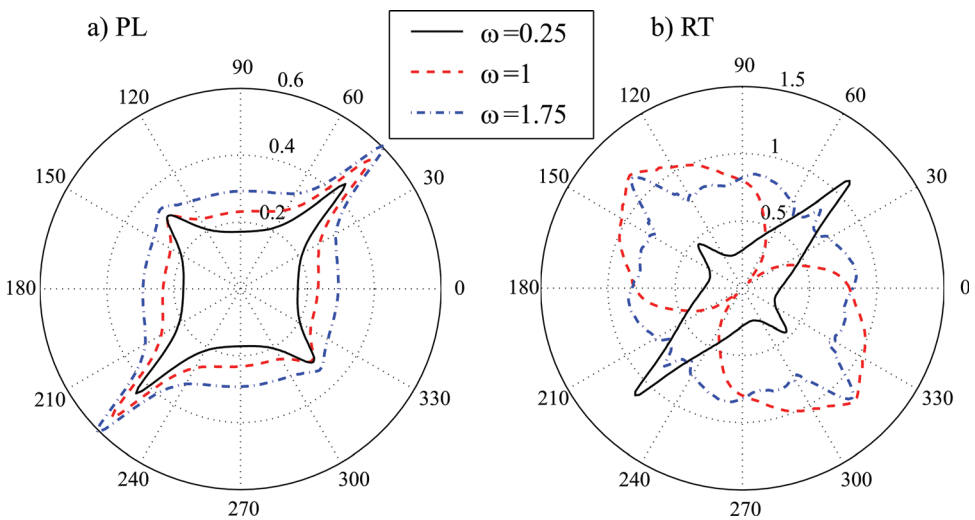

FIG. 6. (Color online) Amplitude diagrams $V_z(\varphi)$ for GWs excited by PL (a) and RT (b) sources in laminate A.

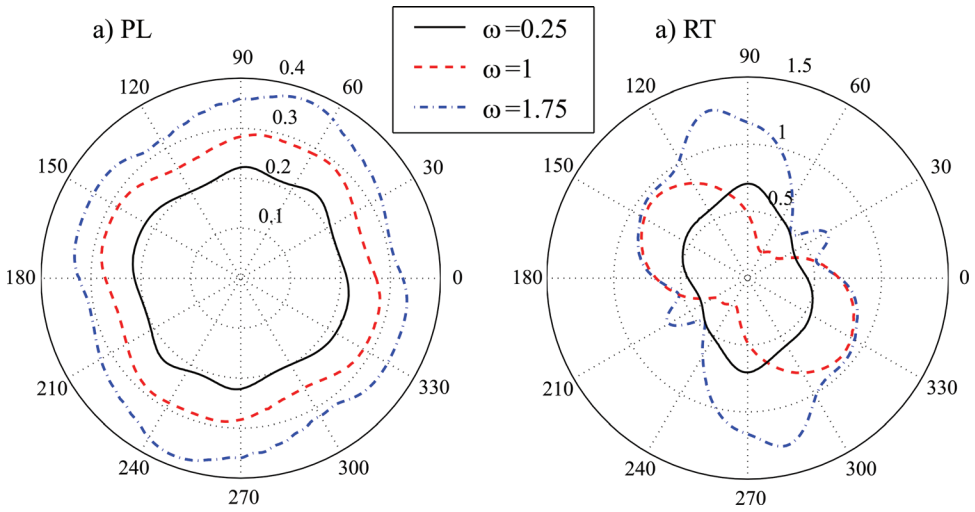

FIG. 7. (Color online) The same as in Fig. 6 but for the eight-layer non-symmetric specimen *B*.

slightly directed signals tending to degenerate into the simple circle diagrams inherent for isotropic plates as the number of sublayers M increases [Fig. 7(a)]. The same tendencies can also be seen in the energy diagrams E(φ) in Figs. 8–10.

Theoretical investigations of wave energy fluxes in anisotropic laminates based on the concept of Gaussian beams are presented in Ref. 9. They are augmented by experimental, laser-based measurements of surface waves. The results obtained for a specimen similar to laminate *A* also demonstrate preferred energy outflow in the direction of the upper-ply fibers ($\varphi = 45°$), with a weaker flux in the orthogonal direction $\varphi = 135°$ connected with the inner-ply orientation [as in Fig. 6(a)]. Test computations for other composite plate parameters[9] gave similar power density patterns. In all cases, laser-generated (point-source) GWs transport the greater part of their total energy in the direction of upper-ply fibers, unlike to GWs actuated by a sized source (e.g., Fig. 9).

Besides, experimental results showing preferable Lamb wave radiation in the fiber directions are presented in recent paper (Ref. 26). As for the theoretical model described in the present paper, it has also been tested against experimental measurements in cooperation with German colleagues.[27]

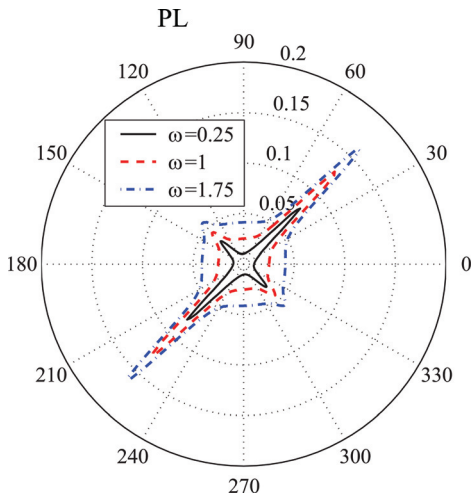

FIG. 8. (Color online) Energy diagrams $E(\varphi)$ for GWs excited by the point-source in laminate *A*.

B. Energy partition

For a better understanding of the main lobe alternation mechanism revealed for sized sources, let us consider wave energy behavior in more detail. The energy conservation law implies that the value $E_0 = \int_0^{2\pi} E(\varphi)d\varphi$ is independent of r and equal to the amount of energy incoming into substrate through the load area Ω over the time period $T = 2\pi/\omega$. It may also be referred to as the source power. With a fixed force applied to a non-point area Ω, the source power E_0 depends not only on frequency and substrate's material properties but also on the Ω size as well. Figure 11 illustrates the dependency of E_0 on a and ω for the RT source bonded to isotropic (a) and anisotropic (b) substrates having the same properties as in Fig. 5. One can see that E_0 maxima and minima (light and dark stripes) follow hyperbolic trajectories $a\omega =$ const. It hints at the existence of certain wavelength-to-source-diameter ratios that are either optimal or unfavorable for the radiation of wave energy from the source to infinity.

This consideration is in agreement with previous 2D analysis for strip piezo-actuators.[28] Based on a strict patch-layer contact problem solution it has been shown that the energy of generated GWs reaches maximal values if the patch width $2a$ is equal to a half-number of its wavelength λ

$$2a/\lambda = k + 1/2, \quad k = 0, 1, 2, \ldots. \tag{42}$$

In such a case, the modes generated by the strip edges $x = \pm a$ are added in-phase, while with the ratio $2a/\lambda = k$ they are out of phase and destructively interfere with each other.

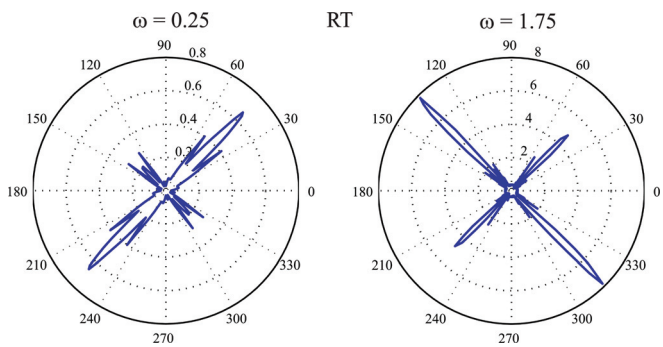

FIG. 9. (Color online) The same as in Fig. 8 but for the circular RT source.

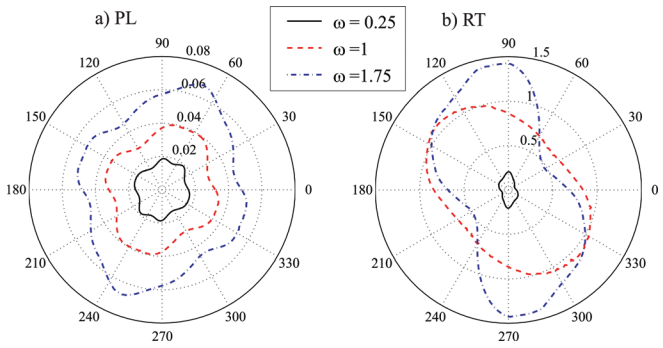

FIG. 10. (Color online) Energy diagrams $E(\varphi)$ for laminate B.

A similar mechanism operates with circular sources. In the isotropic case, the amplitude factors of normal mode asymptotics (30) take the form

$$\mathbf{a}_n(\mathbf{x}) = b_n(\varphi, z)\mathbf{Q}(-\zeta_n, \varphi)$$

and from the explicit $\mathbf{Q}$ representation for the RT source given in Eq. (12) it directly follows that $|\mathbf{u}_n| = 0$ if $a\zeta_n = j_k, k = 0, 1, 2, \ldots$, where j_k are real zeros of the Bessel function J_1: $J_1(j_k) = 0$. If only one mode ζ_1 is in the ω range considered, then Fig. 11(a) would present regular dark stripes along the curves $a\zeta_1 = j_k, k = 1, 2, 3, \ldots$, alternated with white zones of maximal radiated source energy as $a\zeta_1 \approx (j_k + j_{k+1})/2$. With two fundamental modes A_0 and S_0 actually generated in this range, the alternation of such zones is not so regular, being dependent on which of the modes provides the dominate contribution to the total energy E_0. From Fig. 11(a), one can conclude that a border between the areas of A_0 and S_0 energy domination exists in the (a, ω) plane approximately along the line $\omega = a - 4$. With anisotropic laminate A [Fig. 11(b)], the light and dark stripes form a similar pattern, which, however, does not coincide with the pattern for an isotropic plate.

The regularities of the main lobe turnings in the $E(\varphi)$ diagrams may be derived from an analysis of the source energy partition between GWs radiated into the neighboring first and second quadrants

$$E_I = \int_0^{\pi/2} E(\varphi)d\varphi \quad \text{and} \quad E_{II} = \int_{\pi/2}^{\pi} E(\varphi)d\varphi.$$

The energy conservation law results in the balance equality $E_I + E_{II} = E_0/2$. Therefore, it is convenient to evaluate the

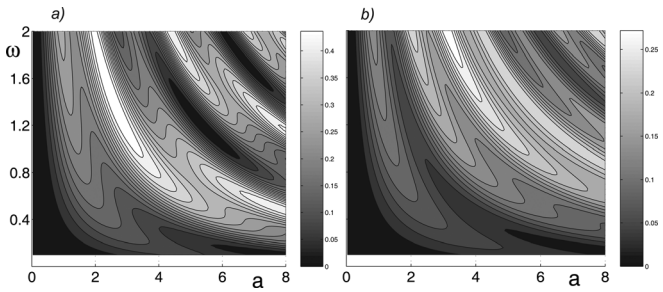

FIG. 11. Source power E_0 as a function of transducer radius a and frequency ω for isotropic plate (a) and anisotropic laminate A (b).

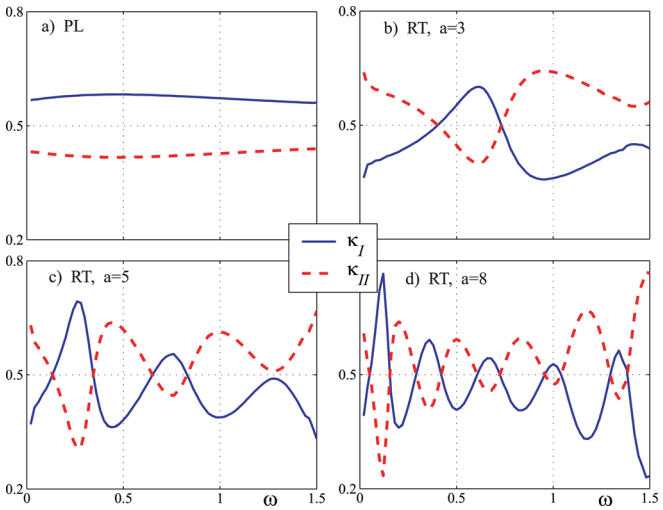

FIG. 12. (Color online) Frequency dependencies of the partition coefficients κ_I and κ_{II} for a PL (a) and for RT of radii $a = 3$, 5 and 8 (b)–(d), laminate A.

partition in terms of the coefficients $\kappa_I = 2E_I/E_0$ and $\kappa_{II} = 2E_I/E_0$ which in sum are equal to unity: $\kappa_I + \kappa_{II} = 1$.

Figure 12 shows their dependence on ω for a PL (a) and for RT of radii $a = 3$, 5, and 8 (b)–(d). One can see that the PL radiates more energy into the first quadrant (i.e., along the fibers of the upper plies) with the energy balance being practically independent of ω. This is in conformity with the PL diagrams in Fig. 8. On the contrary, the RT plots reveal the alternation of the principal direction of radiation associated with both ω and a variation. The larger the source radius a, the more frequent such alternation versus ω becomes. This again points to the existence of optimal ratios $2a/\lambda$ providing maximal energy radiation in the direction of upper fibers $\varphi = 45°$ (i.e., into the first quadrant) and in the orthogonal direction of inner fibers $\varphi = 135°$, similar to Eq. (42).

The mechanism of maximal radiation in a certain direction φ is roughly the same as with strip actuators. It may be explained by an in-phase composition of GWs generated by the opposite edges of the circular RT source at the ends of the φ-oriented diameter. The alternation obviously results from the fact that due to anisotropy the wave length $\lambda = 2\pi/s_{nm}$ is different for different directions of radiation φ. With increasing number of multidirectional sublayers, this difference is less pronounced, therefore, with laminate B, the angular directivity becomes blurry.

VII. CONCLUSION

The mathematical model developed based on the integral equation approach has proved to be an efficient tool for fast computer simulation of GWs generated by a surface force applied to an anisotropic laminate composite plate. The explicit series and the closed-form asymptotic representations derived for 3D Green's matrix from the double path Fourier integrals in terms of cylindrical waves allow one to strictly account for the wave source characteristics. Due to low-cost and clear physical interpretation of the wave characteristics, the model is advantageous for tackling the problems that occur in the physical acoustics of laminate structures and

SHM applications. The method can be useful for the identification of composite plate material parameters from Lamb wave measurements, for the detection and estimation of defects, for a proper choice of excitation frequencies, and for optimal selecting of transducer size and positioning.

ACKNOWLEDGMENTS

We are thankful to Professor R. Lammering, Helmut Schmidt University, Hamburg, for fruitful cooperation, especially in the experimental verification of the theoretical methods and computer models developed. This work is supported by the Russian Ministry for Education and Science, project No. 2.1.1/10463.

[1]W. T. Thomson, "Transmission of elastic waves through a stratified solid medium," J. Appl. Phys. **21**, 89–93 (1950).
[2]N. A. Haskell, "The dispersion of surface waves on multilayered media," Bull. Seismol. Soc. Am. **43**, 17–34 (1953).
[3]G. I. Petrashen, "Propagation of elastic waves in layered isotropic media divided by parallel planes," Uchenye Zapiski Leningradskogo Gosuniversiteta **162**, 3–189 (1952) (in Russian).
[4]A. H. Nayfeh, "The general problem of elastic wave propagation in multilayered anisotropic media," J. Acoust. Soc. Am. **89**(4), 1521–1531 (1991).
[5]J. J. Ditri and J. L. Rose, "Excitation of guided waves in generally anisotropic layers using finite sources," J. Appl. Mech. **61**, 330–338 (1994).
[6]M. J. S. Lowe, "Matrix techniques for modeling ultrasonic waves in multilayered media," IEEE Trans. Ultrason. Ferroelectr. Freq. Control. **42**(4), 525–542 (1995).
[7]E. Moulin, J. Assaad, C. Delebarre, and D. Osmont, "Modeling of Lamb waves generated by integrated transducers in composite plates using a coupled finite element–normal modes expansion method," J. Acoust. Soc. Am. **107**(1), 87–94 (2000).
[8]L. Wang and F. G. Yuan, "Group velocity and characteristic wave curves of Lamb waves in composites: Modeling and experiments," Compos. Sci. Technol. **67**(8), 1370–1384 (2007).
[9]K. Balasubramaniam and C. V. Krishnamurthy, "Ultrasonic guided wave energy behavior in laminated anisotropic plates," J. Sound Vib. **296**, 968–978 (2006).
[10]S. I. Rokhlin and L. Wang, "Ultrasonic waves in layered anisotropic media: characterization of multidirectional composites," Int. J. Solids Struct. **39**, 5529–5545 (2002).
[11]A. Velichko and P. D. Wilcox, "Modelling the excitation of guided waves in generally anisotropic multi-layered media," J. Acoust. Soc. Am. **121**, 60–69 (2007).
[12]B. A. Auld, *Acoustic Fields and Waves in Solids* (Wiley, New York, 1973), Vol. 1, Chap. 7, pp. 191–235.
[13]A. Raghavan and C. E. S. Cesnik, "Review of guided-wave structural health monitoring," Shock Vib. Dig. **39**(2), 91–114 (2007).
[14]A. V. Sveshnikov, "The limit absorption principle for a waveguide," Dokl. Akad. Nauk SSSR [Sov. Phys. Dokl.] **80**(3), 345–347 (1951) (in Russian).
[15]I. Tolstoy and E. Usdin, "Wave propagation in elastic plates: Low and high mode dispersion," J. Acoust. Soc. Am. **29**, 37–42 (1957).
[16]C. Prada, D. Clorennec, T. W. Murray, and D. Royer, "Influence of the anisotropy on zero-group velocity Lamb modes," J. Acoust. Soc. Am. **126**(2) 620–625 (2009).
[17]E. Glushkov, N. Glushkova, M. Golub, and A. Boström, "Natural resonance frequencies, wave blocking, and energy localization in an elastic half-space and waveguide with a crack," J. Acoust. Soc. Am. **119**(6), 3589–3598 (2006).
[18]S. Banerjee, W. Prosser, and A. Mal, "Calculation of the response of a composite plate to localized dynamic surface loads using a new wave number integral method," ASME J. Appl. Mech. **72**(1), 18–24 (2005).
[19]E. Moulin, S. Grondel, M. Baouahi, and J. Assaad, "Pseudo-3D modeling of a surface-bonded Lamb wave source," J. Acoust. Soc. Am. **119**, 2575–2578 (2006).
[20]H. Bateman and A. Erdélyi, *Higher transcendental functions, II* (McGraw-Hill, New York, Inc., 1953); Translated into Russian: (Nauka, Moscow, 1966), Chap. 7, Sec. 7.3.1, Eq. 2.
[21]V. A. Babeshko, E. V. Glushkov, and N. V. Glushkova, "Methods of constructing Green's matrix of a stratified elastic half-space," USSR Comput. Math. Math. Phys. **27**(1), 60–65 (1987).
[22]Ye. V. Glushkov, N. V. Glushkova, A. A. Yeremin, and V. V. Mikhas'kiv, "The layered element method in the dynamic theory of elasticity," J. Appl. Math. Mech. **73**, 449–456 (2009).
[23]H. Schmidt and G. Tango, "Efficient global matrix appraoch to the computation of synthetic seismograms," Geophys. J. R. Astron. Soc. **84**, 331–359 (1986).
[24]A. N. Stroh, "Steady state problems in anisotropic elasticity," J. Math. Phys. **41**, 77–103 (1962).
[25]N. A. Umov, "The equations of motion of the energy in bodies [in Russian]," Odessa (1874), in: *Selected works* (State Publishers of Technical-Theoretical Literature (GITTL), Moscow-Leningrad, 1950); as cited by O.A. Godin, J. Acoust. Soc. Am. **125**(4) (2009), and by A.P. Kiselev, J. Math. Sci. **19**(4), 1372–1375.
[26]B. Chapuis, N. Terrien, and D. Royer, "Excitation and focusing of Lamb waves in a multilayeredanisotropic plate," J. Acoust. Soc. Am. **127**(1), 198–203 (2010).
[27]R. Lammering, A. A. Eremin, E. V. Glushkov, N. V. Glushkova, M. N. Neumann, and B. Hennings, "Experimentelle und numerische Untersuchungen zur Ausbreitung von Lambwellen in dunnen Platten," 17 Workshop Physikalische Akustik (Bad Honnef, Germany), 21–22 October 2010.
[28]E. Glushkov, N. Glushkova, O. Kvasha and W. Seemann, "Integral equation based modeling of the interaction between piezoelectric patch actuators and an elastic substrate," Smart Mater. Struct. **16**, 650–664 (2007).